High spatial resolution ToF-SIMS imaging and image analysis strategies to monitor and quantify early phase separation in amorphous solid dispersions

Eleonora Paladino[a,b,c,1], Frederik J. S. Doerr[a,b,1], Ecaterina Bordos[a,b], Iyke I. Onyemelukwe[a,b], Dimitrios A. Lamprou[d], Alastair J. Florence[a,b], Ian S. Gilmore[c], Gavin W. Halbert[a,b,e,*]

[a] *EPSRC CMAC Future Manufacturing Research Hub, Technology and Innovation Centre, Glasgow, G1 1RD, UK*
[b] *Strathclyde Institute of Pharmacy & Biomedical Sciences (SIPBS), University of Strathclyde, Glasgow, G4 0RE, UK*
[c] *National Centre of Excellence in Mass Spectrometry Imaging (NiCE-MSI), National Physical Laboratory (NPL), Teddington, TW11 0LW, UK*
[d] *School of Pharmacy, Queen's University Belfast, Belfast, BT7 1NN, UK*
[e] *Cancer Research UK Formulation Unit, SIPBS, University of Strathclyde, Glasgow, G4 0RE, UK*

Abstract

Amorphous solid dispersions (ASDs) are formulations with enhanced drug solubility and dissolution rate compared to their crystalline counterparts, however, they can be inherently thermodynamically unstable. This can lead to amorphous phase separation and drug re-crystallisation, phenomena that are typically faster and more dominant at the product's surfaces. This study investigates the use of high-resolution time of flight-secondary ion mass spectrometry (ToF-SIMS) imaging as a surface analysis technique combined with image-analysis for the early detection, monitoring and quantification of surface amorphous phase separation in ASDs. Its capabilities are demonstrated for two pharmaceutically relevant ASD systems with distinct re-crystallisation behaviours, prepared using hot melt extrusion (HME) followed by pelletisation or grinding: (1) paracetamol-hydroxypropyl methylcellulose (PCM-HPMC) pellets with drug loadings of 10–50% w/w and (2) indomethacin-polyvinylpyrrolidone (IND-PVP) ground material with drug loadings of 20–85% w/w. PCM-HPMC

*Corresponding Author
Email address: g.w.halbert@strath.ac.uk (Gavin W. Halbert)
[1] Current address: Pharmaceutical Technology & Development, Operations, AstraZeneca, Gothenburg, Sweden

pellets showed intense phase separation, reaching 100% surface coverage within 1-5 months. In direct comparison, IND-PVP HME ground material was more stable with only a moderate formation of isolated IND-rich clusters. Image analysis allowed the reliable detection and quantification of local drug-rich clusters. An Avrami model was applied to determine and compare phase separation kinetics. The combination of chemical sensitivity and high spatial resolution afforded by SIMS was crucial to enable the study of early phase separation and re-crystallisation at the surface. Compared with traditional methods used to detect crystalline material, such as XRPD, we show that ToF-SIMS enabled detection of surface physical instability already at early stages of drug cluster formation in the first days of storage.

Keywords: chemical imaging, time of flight-secondary ion mass spectrometry (ToF-SIMS), pharmaceutical solid products, amorphous solid dispersion (ASD), surface physical stability, amorphous phase separation, surface-enhanced re-crystallisation, crystal nucleation, crystal growth, hot melt extrusion (HME)

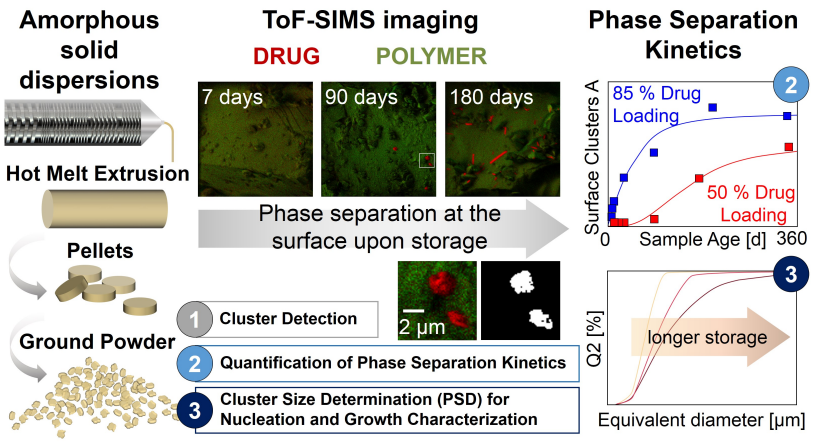

Graphical abstract.

1. Introduction

Due to their advantageous characteristics, amorphous solids have widespread technical applications in different industries, Amorphous solids have unique properties which are utilised for a wide range of applications, including energy storage [1, 2, 3], semiconductors [4, 5], structural materials [6, 7, 8] and pharmaceuticals [9, 10]. In the pharmaceutical industry, poorly water-soluble active pharmaceutical ingredients (APIs) are often rendered amorphous to exploit the enhanced solubility and dissolution rate associated with the amorphous state [9, 10]. The increased drug solubility [11, 12] significantly enhances the APIs bioavailability after oral administration in those specific cases where the drug presents high permeability, and thus solubility is the limiting step hindering absorption [13] (Class II of the Biopharmaceutical Classification System, BCS [14]). APIs can be rendered amorphous either as a single component or, more frequently, with a carrier polymer as multi-component amorphous solid dispersions (ASDs) [15]. The selection of a suitable polymer, API/polymer ratio and manufacturing conditions are crucial to obtain kinetically-stabilised ASD systems.

The main disadvantage of the amorphous state is its inherent thermodynamic instability, and hence its propensity to convert into an energetically favourable crystalline form. Despite being kinetically stabilised, for ASDs this can lead to amorphous phase separation (APS) or drug re-crystallisation phenomena, hampering long-term stability of this type of formulation [16, 17]. Previous studies conducted on amorphous pharmaceutical solids have highlighted that re-crystallisation phenomena can occur orders of magnitude faster at the surface of amorphous compounds than in the bulk [18, 19]. Specific examples of surface-enhanced APS/re-crystallisation have been reported also for ASDs [20, 21]. The assessment of solid phase stability and re-crystallisation kinetics of ASDs is

crucial to ensure the maintenance of product efficacy and quality throughout its shelf life. Hence, there is an opportunity for an early detection of phase separation effects through an investigation focused on the sample surface, which could consequentially also save time and costs during formulation development [22].

Commonly used techniques to evaluate physical stability of ASDs are differential scanning calorimetry (DSC) and X-ray powder diffraction (XRPD) [15, 23, 24, 25]. Their sensitivity is insufficient to detect nanocrystalline domains [26] or crystalline content below 1-5% [27, 15, 28]. Solid-state nuclear magnetic resonance (ssNMR) can be utilized to quantify <1% crystallinity [29]; however, data acquisition is time-consuming and, equally to DSC and XRPD, ssNMR does not provide spatially resolved information, which makes these techniques thus unable to differentiate between surface and bulk crystallinity. To date, only a few analytical techniques have been used with the express aim of assessing surface stability of ASDs, namely confocal Raman microscopy (CRM) [30], scanning electron microscopy (SEM) used together with attenuated total reflectance-Fourier transform infrared spectroscopy (ATR-FTIR) [31] or AFM combined with infrared spectroscopy (AFM-IR) and thermal analysis [32, 33]. These analytical techniques, however, have limitations towards their ability to provide local chemical information for identification or their achievable spatial resolution, and drawbacks associated with destructive sample preparation and/or analysis cycles, method-specific sample requirements (e.g. thin films with homogeneous thickness and surfaces without significant topographical features), long data acquisition and/or acquisition limited to a small sample area. This entails the use of multiple complementary techniques for a conclusive characterisation of surface physical instability.

Time of flight-secondary ion mass spectrometry (ToF-SIMS) is a high spatial

resolution (< 200 nm [34, 35]) chemical imaging technique which has high surface specificity (information depth of 3-5 nm using a 25 kV Bi_3^+ [36]). ToF-SIMS imaging is significantly less time consuming than Raman mapping and AFM-IR working at comparable resolution and image size. ToF-SIMS requires no or very limited sample preparation, enabling the analysis of native surfaces of finished pharmaceutical solid products. For instance, it was used to characterize local surface composition in spray-dried powders, which provided insights into the particle formation process during drying [37, 38]. Furthermore, ToF-SIMS has been employed effectively in the past to characterise local phase separation of ASDs and its impact on the products' performance, e.g. drug-release behaviour in electrospun drug delivery systems [39, 40], although not with the aim to provide kinetic information through a long-term physical stability study. ToF-SIMS is not *per se* established for the characterisation of the materials' solid state, however it was demonstrated that ToF-SIMS can be used to successfully differentiate between amorphous and re-crystallised regions in amorphous mono-compound material obtained via quench melting, with the support of multivariate analysis (MVA) strategies [41]. The beneficial use of ToF-SIMS imaging in an industrial context was highlighted in recent research, where ToF-SIMS and MVA were employed to quantify surface coverage of selected ingredients on carrier powders for inhalation, providing insights on key-mechanisms of the blending process and ultimately enabling a control of the product performance [42, 43].

Image processing and analysis (IP&A) is regularly performed in combination with imaging techniques to assist the interpretation of collected data and to extract (semi-) quantitative sample information. In the pharmaceutical field, successful applications of IP&A range from 2D to 3D image data characterisation of systems such as crystals, particles, capsules and tablets [44, 45, 46, 47].

For ToF-SIMS there have been significant improvements in image processing to translate the raw spectral data from complex multicomponent samples to images visualising the spatial distribution of individual chemical compounds [48, 42, 43] or highlighting subtle changes in the spectra related to the material solid state [41]. The additional use of image analysis methodologies provides a means for automated, high-throughput and objective evaluation of ToF-SIMS chemical images, in contrast to manual measurements that are less time-effective, have a lower throughput and may be subjective and biased.

In this study, we assess the use of high spatial resolution ToF-SIMS imaging to detect and monitor surface amorphous phase separation and re-crystallisation for two distinct bicomponent ASD systems manufactured through hot melt extrusion (HME). After HME, one system was pelletised and one was ground. These are two processing steps commonly applied to extruded material in the pharmaceutical industry [15]. The two compound systems were selected because of their different surface re-crystallisation behaviours, which enabled the development of a comprehensive chemical imaging and IP&A work-flow, with potential applicability to a wider range of ToF-SIMS image data. The developed and implemented IP&A routine permits the automated extraction of quantitative information on dimensions, number and surface coverage of API-rich domains, and hence the ability to study different aspects of the surface APS/re-crystallisation kinetics for ASD systems over a period of up to one year, providing crucial insights on the stability of these systems. ToF-SIMS imaging enables detection of API-rich domains, comprising both phase-separated clusters and already-formed crystals. This provides a significant time advantage compared to established techniques used to detect solid-state instability which are instead based on the detection of already-formed crystals (above a certain threshold of crystallinity content), such as XRPD.

2. Materials and Methods

2.1. Chemicals

Pharmaceutical grade paracetamol was sourced from Mallinckrodt Inc. (Raleigh, USA). Hydroxypropyl methylcellulose grade Affinisol^{TM} 15LV was kindly donated by Dow Inc. (The Dow Chemical Company, Michigan, USA). Crystalline $\gamma - polymorph$ indomethacin of purity $\geq 98.5\%$ and polyvinylpyrrolidone grade PVP Kollidon® 25 were purchased from Sigma-Aldrich (Dorset, UK). Skeletal structural formulae and repeat units of the chemicals used in the study are illustrated in Fig. S1.

2.2. Hot melt extrusion (HME)

Four powder blends of paracetamol (PCM) and hydroxypropyl methylcellulose (HPMC), with weight ratios of 10:90 (PCM-C10), 20:80 (PCM-C20), 35:65 (PCM-C35) and 50:50 (PCM-C50) w/w PCM/HPMC, were prepared in a 5L AgiBlend bin blender (Pharmatech, UK) at set blend speed of 25 rpm and agitation of 500 rpm for 20 minutes. HME was performed using a Thermo Scientific^{TM} Process 11 Parallel Twin-Screw Extruder (Thermo Scientific, UK) equipped with co-rotating twin screws and a 1.8 mm diameter round die nozzle. Pre-blend binary mixtures were fed with a loss-in-weight gravimetric feeder (Brabender Technologie, Germany) at a feed rate of 0.1 kg/h for all systems. The extrusion temperatures were selected as described by Bordos *et al.* [49] to produce fully amorphous extrudates as characterized using in-line terahertz-Raman spectroscopy and confirmed through off-line DSC measurements. PCM-C10, PCM-C20 and PCM-C35 were extruded at 150°C, PCM-C50 at 155°C. For all systems, the rotating speed of the screws was set to 100 rpm. Once cooled down, filaments were pelletized with a Thermo Scientific^{TM} VariCut Pelletizer (Thermo Scientific, UK). Pellets with height and diameter of approximately 2

mm were mounted exposing the freshly obtained surface on the sample stage for subsequent SIMS analysis. After analysis, the pellets were stored at room temperature (23.0±0.3°C) in a desiccator until the following stability time-point. Indomethacin (IND) and polyvinylpyrrolidone (PVP) powder blends were produced with w/w ratios of 20:80 (IND-C20), 50:50 (IND-C50), 70:30 (IND-C70) and 85:15 (IND-C85) w/w IND/PVP, using the same conditions as described for the PCM-HPMC system. A Thermo Scientific^{TM} Pharma 16 Twin-Screw Extruder (Thermo Scientific, UK) was operated at 175°C and mounted a round die of 1 mm diameter. The screw speed was 100 rpm and the dwell time was 1.2 minutes. HME material was ground in a controlled relative humidity (RH) glove bag (Aldrich® AtmosBag, Sigma-Aldrich, UK) filled with N_2, at 3% RH, at room temperature and for approximately 4 minutes, until a homogeneous powder was obtained. Intact extrudate strands and ground material were stored at room temperature (23.0±0.3°C) and 32.6±1.7% RH, in sealed glass vials. An overview of all PCM-HPMC and INDPVP included in this study is provided in Table S1.

2.3. ToF-SIMS high spatial resolution imaging

SIMS reference spectra and high spatial resolution images of the two systems were acquired using an IONTOF TOF.SIMS 5 instrument (IONTOF GmbH, Münster, Germany), equipped with a bismuth liquid metal ion gun (LMIG) and a gridless reflectron time-of-flight mass analyser. All SIMS analyses were recorded using SurfaceLab software packages (versions 6.7, 6.8 and 7, IONTOF GmbH, Münster, Germany). Strategies proposed by Lee *et al.* [50] were applied to reduce topographic field effects and improve the charge compensation on the insulating samples. Validation optical microscopy images were acquired with a Leica DM6000 M microscope (Leica Microsystems GmbH, Germany).

2.3.1. PCM-HPMC pellets

An unbunched 30 keV Bi_3^+ primary ion beam was used to acquire high spatial resolution secondary ion images on PCM-HPMC pellets (PCM-C10 - PCM-C50) over a 500 µm × 500 µm field of view (FoV). The analyses were conducted in randomly selected locations on the surface of the pellets. For the time-points following the first, additional images were collected on the same location to visually assess growth of the API-rich domains. These were excluded from the quantitative evaluation of surface coverage kinetics to eliminate the risk of the ToF-SIMS analysis impacting on local kinetics. The primary ion dose (PID), spatial resolution and pixel width were respectively 2×10^{11} (primary ions/cm^2), 0.55 µm and 0.49 µm. Within the 500 µm × 500 µm FoV, two additional 100 µm × 100 µm images were acquired, using an unbunched 60 keV Bi_3^{2+} primary ion beam for improved spatial resolution, and delivering a PID of 5×10^{11} (primary ions/cm^2). For these images the spatial resolution and pixel width were 0.15 µm and 0.099 µm, respectively. The mass spectral information was collected in the positive secondary ion polarity with a 0.055 µs delayed extraction. The mass range was recorded between 0 and 900 Da and was calibrated using the CH_3^+, $C_2H_3^+$, $C_3H_7^+$, $C_4H_9^+$, $C_4H_9O^+$ (HPMC) and $C_8H_{10}NO_2^+$ (PCM, $[M+H]^+$) secondary ions, as recommended by Green *et al.* [51].

2.3.2. IND-PVP ground powder

Samples of the ground material (IND-C20 - IND-C85) were transferred from the stored powder and fixed on the ToF-SIMS sample holder on the day of analysis. The characterisation frequency of the ground material was selected depending on the expected re-crystallisation kinetics, aiming to provide sufficient time-resolution to quantify early APS/re-crystallisation of ASDs with high drug loadings. Immediately prior to transfer in the instrument air lock,

extruded glass samples were broken in order to generate new surfaces, and individual pieces were secured on the ToF-SIMS sample holder, exposing the freshly created surfaces for analysis and limiting their exposure to air to less than 5 minutes. A 60 keV Bi_3^{2+} primary ion beam was operated in unbunched mode to collect high spatial resolution secondary ion images of selected areas on the surface of the HME material and of the ground particles (spatial resolution $<$ 300 nm, pixel width of 0.12 µm). Each acquisition was performed over a FoV of 60 µm $\times$ 60 µm, a value which was close to the particle size (diameter 2D projection), in order to ensure the fit of single particles in the FoV. The total PID delivered for each image was approximately 5×10^{11} (primary ions/cm^2). The analyser extraction delay was set to 0.055 µs to improve mass-resolving power and to reduce topographic field effects. The mass spectral information was recorded in the positive secondary ion polarity, in the mass range of 0–900 Da and calibrated using the CH_3^+, $C_2H_3^+$, $C_3H_7^+$, $C_4H_9^+$, $C_6H_{10}NO^+$ (PVP, $[M_{monomer}+H]^+$), and $C_{19}H_{16}ClNO_4^+$ (IND, $[M]^+$) fragment ions. The analysis was repeated on a minimum of 4 particles for each system at each time-point.

2.4. Image processing for the detection and quantification of surface APS/ re-crystallisation

SIMS images were used to extract quantitative data, such as dimensions and number of distinct surface API-rich domains and their overall surface coverage, in order to evaluate the kinetics of surface APS/re-crystallisation. For this purpose, the SIMS data were exported and further processed using custom scripts developed in MATLAB 2019 (The MathWorks, Inc. USA). Selected steps of the SIMS image processing workflow are visualised in Fig. 1.

Identification and putative assignment of diagnostic peaks for each compound enabled reconstruction of API-polymer colour overlay images (Fig. 1 A). SIMS spectral data were exported to generate greyscale images of the API and the

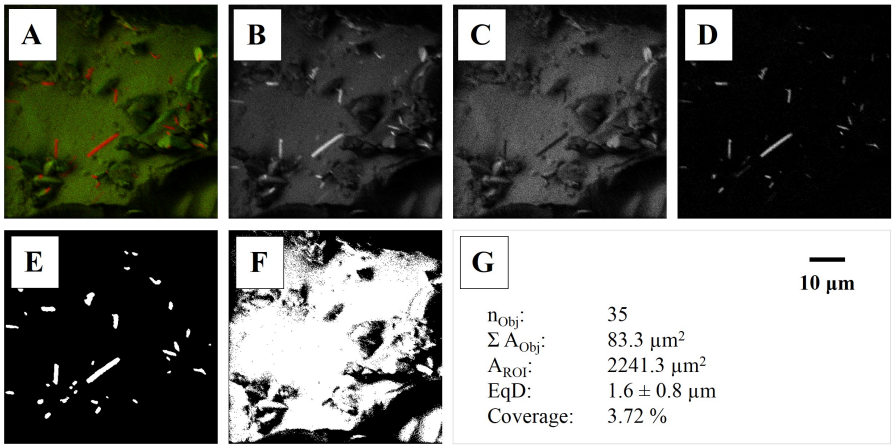

Figure 1: Image processing steps applied to SIMS data for the detection and quantification of API-rich domains related to surface APS/re-crystallisation. (A) Constructed color overlay with (red) API and (green) polymer dominated domains. (B-C) Single component images for API (I_{API}) and polymer (I_{Pol}) with normalised ion counts, (D) image subtraction of I_{API} and I_{Pol} generating the API-rich domain image (I_{API-R}), (E) binary image after thresholding and noise reduction ($I_{API-R,BIN}$), (F) total effective area containing intensity information (ROI), (G) results of the object detection method with measured number (n_{Obj}), area (ΣA_{Obj}) and equivalent circle area diameter (EqD) of the objects, area of ROI (A_{ROI}) and % drug coverage ($\Sigma A_{Obj}/A_{ROI}$).

polymer distribution (I_{API} and I_{Pol}, Fig. 1 B-C). After applying an ion-yield correction factor based on the median count in each of the two greyscale images to adjust for differences in the count intensities between distinct chemical entities, the I_{Pol} was subtracted from the I_{API}, generating the API-rich domain image (I_{API-R}, Fig. 1 D). Random noise was reduced by applying an edge-preserving median filter and an adaptive low pass Wiener filter within a 3×3 and 11×11 pixel kernel, respectively. The I_{API-R} was converted to a binary image using a fixed threshold (of 0.039 for IND, 0.247 for PCM) to enable the subsequent comparison of detected API-rich domains. A cluster size threshold of 10 pixels and an opening-by-reconstruction step with a 2 × 2 pixel structuring element were applied to remove any potential binary image noise ($I_{API-R,BIN}$, Fig. 1 E). IP&A parameters for thresholding and noise reduction as part of the cluster

detection method were user-validated through a visual comparison of Fig. 1 E with the polymer-API overlay image in Fig. 1 A. Due to topographic effects related to the roughness of the ground material's surface, the effectively analysed surface area in the FoV containing sufficient intensity information was defined as the image region-of-interest (ROI). The ROI in each image was determined after analysing the mean local standard deviation (σ_l) of the pixel intensities in the total ion image within a 5 $\times$ 5 pixel kernel (ROI = I(x,y) $> \sigma_l * 3$, Fig. 1 F). Its value (A_{ROI} in Fig. 1 G) was used to normalise the area occupied by the drug and determine the drug coverage (ΣA_{Obj} and Coverage in Fig. 1 G). For the IND-PVP system, detected API-rich domains were well-defined and separated which allowed the additional quantification of their number (n_{Obj}) and size (EqD). For each cluster, the diameter of a circle having equivalent area (EqD) was calculated. The EqD values and the API surface coverage area were used to generate and track changes in the particle size distributions (PSDs). For the PCM-HPMC systems, which presented adjoining drug clusters in the SIMS images, n_{Obj} and EqD were not determined.

2.5. Kinetics of surface APS/re-crystallisation

The classic Avrami model [52, 53, 54] is frequently used to describe phase transition mechanisms such as crystallisation. In this model, the relative crystalline fraction ($\alpha_s(t)$) is correlated with the storage time (t) according to Equation 1:

$$\alpha_s(t) = 1 - \exp[-k \cdot t^{n_A}] \tag{1}$$

where k is the re-crystallisation rate constant and the Avrami exponent (n_A) is a constant reflecting the nucleation rate and/or the dimensionality of crystal growth. The exponent n_A takes on values between 1 and 4 and can be interpreted as $n_A = Dim + 1$, where Dim represents the dimensionality of crystal growth and 1 is the contribution of crystal nucleation. In the present

study, Equation 1 was used to quantify kinetics of amorphous phase separation and re-crystallisation for cases where growth was predominant over nucleation, and further assuming diffusion controlled crystal growth kinetics of needle and plate-like structures ($n_A = 1$) [55].

The classical Avrami model assumes a constant nucleation rate (J_0) for the phase transition, which, however, does not apply in cases where the available nucleation sites and the amorphous fraction ($1 - \alpha_s(t)$) decrease significantly throughout the re-crystallisation process, leading to an over-prediction of phase transformation rates [56]. Yang *et al.* [56] derived a modified version of the Avrami model accounting for non-constant nucleation rates (Equation 2) and proposed that the nucleation rate $J(t)$ is proportional to the total amorphous fraction ($1 - \alpha_s(t)$).

$$\alpha_s(t) = 1 - \frac{1}{1 + k \cdot t^{n_A}} \tag{2}$$

where the re-crystallisation rate constant (k) is related to the nucleation rate constant (J_0) and crystal growth rate constant (β). For conditions of homogeneous nucleation n_A assumes values of 2 for rod, 3 for plate and 4 for spherical geometry (with Dim equal to 1 for mono-dimensional growth in rods, $Dim = 2$ for bi-dimensional plate growth and $Dim = 3$ for three-dimensional growth conditions). In the present study, Equation 2 was applied to calculate the re-crystallisation rate constants (k) considering plate-like crystal growth and homogeneous nucleation ($n_A = 3$).

2.6. X-ray powder diffraction (XRPD)

For both systems, X-ray powder diffraction (XRPD) data were acquired at sample-specific time-points during storage to qualitatively evaluate the presence of crystalline material. XRPD data were acquired on the PCM-HPMC pelletised, stored amorphous solid dispersions on the day of extrusion and after

7 days (PCM-C50), 30 days and 150 days (PCM-C10, PCM-C20, PCM-C35) of storage, placing the samples in a 28-position plate mounted on a Kapton® polyimide film (7.5 µm thickness). XRPD data were acquired on the IND-PVP ground, stored amorphous solid dispersions after 1 month, 7 months and 22 months of storage, transferring approximately 5 mg of the powder samples into a glass capillary.

The samples were analysed employing a D8 ADVANCE diffractometer (Bruker AXS GmbH, Germany). X-rays were generated from a copper source with Johansson monochromator (Cu Kα1, λ = 1.541Å, 40 kV × 50 mA). Scattered light was collected in the 2θ range 4° - 35° (step size 0.017°, integration time 2 sec) for the PCM-HPMC and in the 2θ range 3° - 40° (step size 0.017°, integration time 10 sec) for IND-PVP. Reference XRPD patterns were exported from the Cambridge Crystallographic Data Centre (CCDC) database as follows: file HXACAN01, deposited by Haisa *et al.* [57], for crystalline paracetamol polymorphic form I and file INDMET, deposited by Kistenmacher and Marsh [58], for crystalline indomethacin polymorphic form gamma ($\gamma - IND$).

3. Results

3.1. Surface APS/re-crystallisation on PCM-HPMC pellets

For the PCM-HPMC system, all pelletised extrudate samples were transparent after HME and post-processing indicating the successful manufacturing of ASD pellet samples. The spatial distribution of PCM and HPMC across the pellets' surfaces was subsequently studied as part of a ASD stability study selecting diagnostic ion-peaks with distinctive *mass-to-charge* ratio (*m/z*) assigned to each component of the formulation. In particular, PCM was identified by its protonated molecular ion $C_8H_{10}NO_2^+$ at *m/z* 152.07 and by the fragments $C_6H_8NO^+$ (*m/z* 110.06), $C_6H_7NO^+$ (*m/z* 109.05) and $C_5H_6N^+$ (*m/z* 80.05),

whilst HPMC exhibits the characteristic secondary ions $C_4H_9O^+$ (m/z 73.07), $C_3H_7O^+$ (m/z 59.05) and $C_2H_5O^+$ (m/z 45.03), which were not present in the reference spectra for PCM. Positive polarity ToF-SIMS spectra of the reference materials are available in Fig. S2. An extensive list of putative peak assignments is included in Table S2.

Selected ToF-SIMS images from all four investigated drug loadings (PCM-C10, PCM-C20, PCM-C35 and PCM-C50) are gathered in Fig. 2A. PCM-C10 did not present any physical changes at the surface related to detectable PCM- HPMC phase separation within the 150 days of ageing (Fig. 2A, first row), but the samples contained Na^+ (m/z 22.99) high-intensity regions that can be attributed to crystalline NaCl (distribution shown in blue). NaCl is a known impurity in Affinisol^{TM} 15LV. Na^+ clusters were not visible in the other PCM-HPMC systems, which present a lower w/w% concentration of Affinisol^{TM} 15LV. However, APS/re-crystallisation of PCM-rich domains were detected for all higher drug loadings starting from the first analysed time-points (Fig. 2A, second to fourth row). From a qualitative comparison of PCM-C20, PCM-C35 and PCM-C50, it can be noted that at each given time-point the surface coverage increases with increasing drug loading.

The values of surface coverage of PCM-rich domains for each PCM-HPMC system over 150 days of storage are plotted in Fig. 2B ($n_{Img} > 3$). The two samples with the highest drug loadings in this study, PCM-C35 and PCM-C50, exhibit an intense PCM surface APS/re-crystallisation, with a surface coverage of 91% and 87%, respectively, after approximately 30 days of storage. Furthermore, PCM-C35 and PCM-C50 show evidence of surface physical instability as early as 1 day after HME manufacturing (Fig. 2A) which are visible in the form of distinct micrometre-sized PCM-rich domains. These PCM-rich domains later grow to larger structures that resemble agglomerates of crystallites, however, lo-

cal nucleation of new PCM-rich domains still occurs simultaneously even after 14 days of storage (images provided in Fig. S3 and Fig. S4). The plate-like crystals forming on PCM-C20 and PCM-C35 correspond to the monoclinic Form I (stable form). This was observed qualitatively through ToF-SIMS as well as optical microscopy (images included in Fig. S3) and confirmed by XRPD (Fig. S7).

XRPD data collected on the PCM pellet samples show the presence of crystalline material as early as 7 days after manufacturing and upon storage for PCM-C50, whilst PCM-C20 and PCM-C35 continue to exhibit the diffuse halo typical of amorphous material for up to 5 months of storage (X-ray diffraction patterns available in Fig. S7). In comparison, ToF-SIMS high spatial resolution imaging enabled the initial detection of physical instabilities (*i.e.* sub-micron PCM-rich domains) already after less than 24 hours from HME manufacturing for PCM-C50 and PCM-C35, and after 3 days of storage for PCM-C20. This suggests that the total sample crystallinity remains below the XRPD detection limit of 1-5% w/w within this early time-window [27] with a potential predominant effect of PCM-rich domain formation on the exposed sample surface.

The quantified surface coverage for each individual sample shown in Fig. 2B was fitted using the classical Avrami model (Equation 1) and its derived version accounting for non-constant nucleation rate (Equation 2). PCM-C10 was excluded from the fitting approach since no PCM-clusters or crystals were detected. PCM-C20 and PCM-C35 are best interpolated by a sigmoidal curve (Equation 2 with $n_A = 3$), which is composed by an initial onset, a second phase of significant increase in the coverage, and a final stage during which the coverage slowly maximises reaching a plateaux. The inflection point can be interpreted as the end of a nucleation-dominated stage and the beginning of a growth-dominated stage. The onset period can be explained as an induction phase during which *nuclei* that promote crystallisation are forming. For the

PCM-C50 system this onset is not observed and a logarithmic curve (Equation 1 with $n_A = 1$) best describes the data. This indicates that *nuclei* are already present from the initial time-point and start growing directly. In these conditions, growth becomes dominant and further nucleation contributes less to the overall increment of the drug coverage. The kinetic constants of the Avrami model were $k_{\mathrm{PCM-C20}}$ of $1.85 \cdot 10^{-5}\mathrm{d}^{-1}$ (n=3), $k_{\mathrm{PCM-C35}}$ of $4.89 \cdot 10^{-4}\mathrm{d}^{-1}$ (n=3) and $k_{\mathrm{PCM-C50}}$ of $8.35 \cdot 10^{-2}\mathrm{d}^{-1}$ (n=1) for PCM-C20, PCM-C35 and PCM-C50, respectively. No APS/crystallinity was detected for PCM-C10.

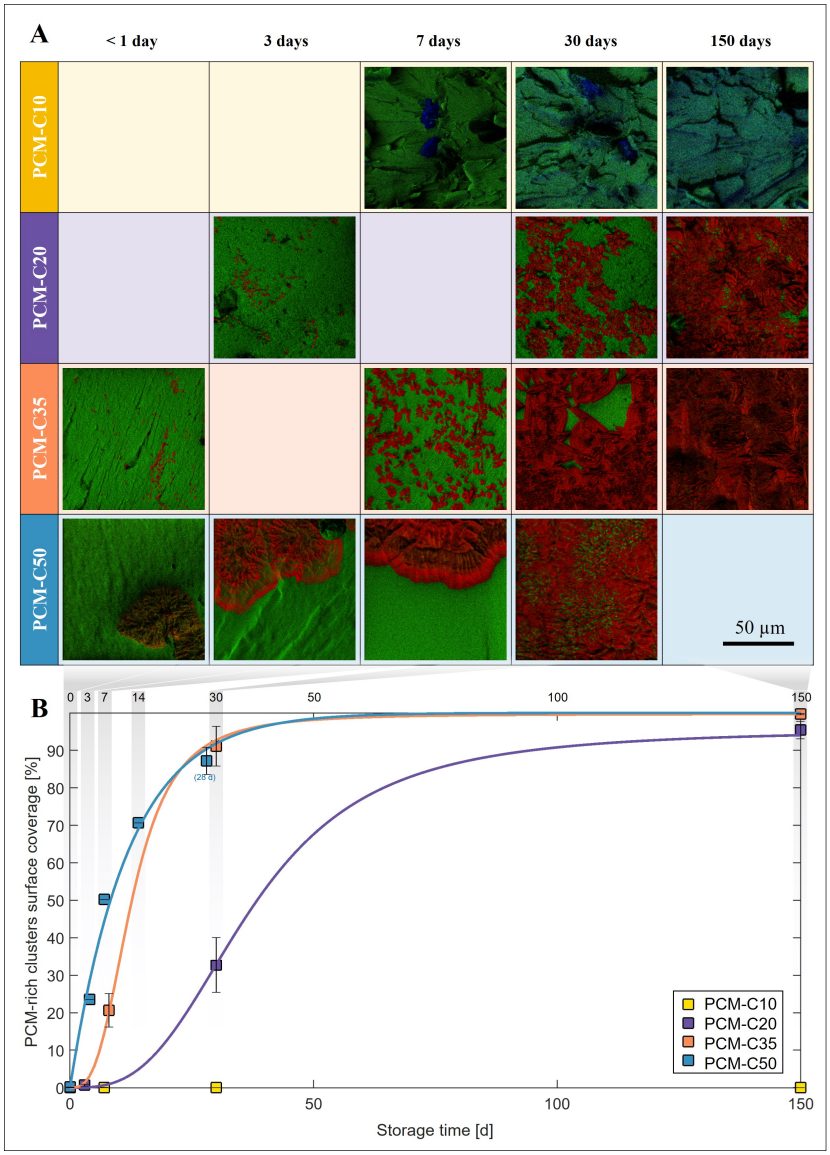

Figure 2: (A) Representative colour-overlay ToF-SIMS images acquired on PCM-HPMC pellets for the systems PCM-C10, PCM-C20, PCM-C35 and PCM-C50 at time-points up to 150 days. PCM (identified by $C_8H_{10}NO_2^+$, $C_6H_8NO^+$, $C_6H_7NO^+$, $C_5H_6N^+$) is displayed in red, HPMC ($C_4H_9O^+$, $C_3H_7O^+$, $C_2H_5O^+$) in green and Na^+ in blue. PCM and HPMC corresponding greyscale images are provided in Fig. S5 and Fig. S6. (B) Quantified PCM surface coverage over the investigated storage time. Error bars represent standard deviation from multiple ToF-SIMS images acquired on individual pellets ($n_{Img} > 3$). PCM-C10 shows no or low tendency for re-crystallisation.

3.2. Surface APS/re-crystallisation on IND-PVP ground powder

In the case of IND-PVP, the produced filaments of all drug loadings were transparent after extrusion and cooling, visually suggesting the absence of crystalline content and the production of a homogeneous amorphous dispersion.

ToF-SIMS imaging was subsequently used to monitor and assess the APS/re-crystallisation kinetics on the surface of IND-PVP samples. IND was identified by the protonated molecular ion $C_{19}H_{17}ClNO_4{}^+$ (*m/z* 358.09), by the fragments $C_7H_4ClO^+$ (*m/z* 138.995) and $C_6H_4Cl^+$ (*m/z* 111.00), and by the corresponding ^{37}Cl isotopes ($C_{19}H_{17}{}^{37}ClNO_4{}^+$ at *m/z* 360.08, $C_7H_4{}^{37}ClO^+$ at *m/z* 140.99, $C_6H_4{}^{37}Cl^+$ at *m/z* 113.00), whereas PVP by the secondary ions $C_6H_{10}NO^+$ (*m/z* 112.08), $C_5H_8NO^+$ (*m/z* 98.06), $C_4H_8NO^+$ (*m/z* 86.06) and $C_4H_5O^+$ (*m/z* 69.03). Positive polarity ToF-SIMS spectra of the references, showing the selected characteristic peaks, are available in Fig. S8. A more extensive list of putative peak assignments is included in Table S4.

In order to further compare the impact of individual post-processing steps during ASD production, data for the IND-PVP system were collected directly after pelletisation of the HME filaments, as well as after pelletisation and grinding. Fig. 3 shows representative images acquired after 6 months of storage on (A) the stored, freshly pelletised, extrudate glass, (B) the pelletised, stored *as pellet*, extrudate glass and (C) the ground, stored, extrudate powder for the IND-C70 system. Samples from the stored but freshly pelletised ASD extrudate give an indication on the APS/re-crystallisation tendency of the ASD bulk in absence of post-processing steps after HME. The pelletised, stored *as pellet* and the ground ASD extrudate samples allow an investigation on the impact of further material processing after HME, with significant differences in the experienced mechanical stress and final specific surface area.

As visible in the colour overlay images in Fig. 3 A and B, the stored extrudates

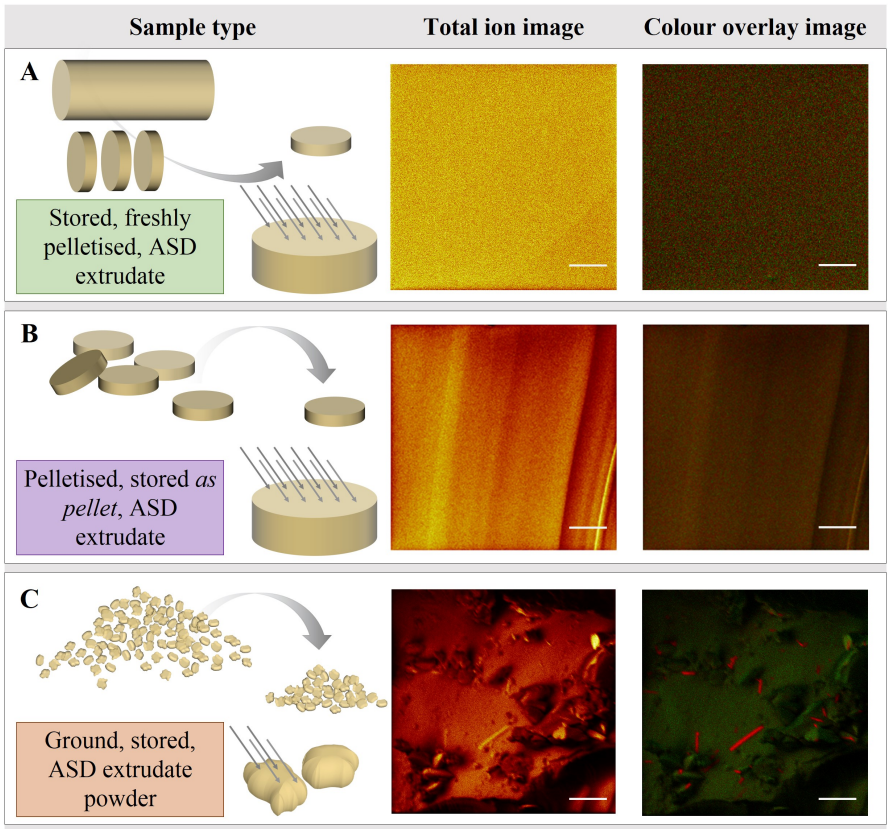

Figure 3: Sample preparation schematics and representative SIMS results for the IND-C70 system after 6 months of storage. ToF-SIMS total ion images and red-green colour-overlay images allow a visualisation of the surface topography and IND-PVP distribution. In the colour-overlay images, IND (identified by $C_{19}H_{17}ClNO_4^+$, $C_{19}H_{17}{}^{37}ClNO_4^+$, $C_7H_4ClO^+$, $C_7H_4{}^{37}ClO^+$, $C_6H_4Cl^+$, $C_6H_4{}^{37}Cl^+$) is shown in red, PVP ($C_6H_{10}NO^+$, $C_5H_8NO^+$, $C_4H_8NO^+$, $C_4H_5O^+$) in green. Scale bar represents 10 µm. (A) Pellets with freshly exposed sample surface from stored extrudate and (B) stored, pelletised extrudate samples appear to have a homogeneous distribution of IND and PVP. (C) Particles from extrudate ground powder present IND-rich domains, indicating amorphous phase separation and re-crystallisation.

that were freshly pelletised after storage and the pelletised, stored *as pellet* material exhibit a uniform distribution of drug (red) and polymer (green), suggesting that the amorphous dispersion remains stable and homogeneous in the extrudate glass form (unground), both in the bulk and at the surface. This was observed for all produced drug loadings in extrudate glass samples and throughout the 12 month investigated storage time period, with additonal color overlay images provided in Fig. S9. In contrast, the ToF-SIMS analysis of the ground material (Fig. 3 C) exhibited an inhomogeneous distribution of the two components, with the presence of well-defined and distinct IND-rich domains indicating significant phase separation during storage. The morphology and the extent of phase separation of these IND-rich domains suggest crystal formation on the surface of the ground material. The rhombic prism ("block-like") crystal lattice is characteristic of the most thermodynamically stable form of IND, *i.e.* $\gamma-$IND ($\gamma - polymorph$, Form I) [59], while the "needle-like" objects might be examples of the $\alpha-polymorph$ (Form II), a metastable form which can however be observed in ambient conditions [60], and reliably isolated [59]. In general, the faster APS/re-crystallisation observed for the powder samples compared to the glass samples might be the result of expected differences in the surface roughness between both systems and the applied mechanical stress during the grinding process [61].

Representative ToF-SIMS images of the ground material for IND-C70 and IND-C85 which were acquired throughout the stability study are collated in Fig. 4A. The API distribution is displayed in red and the polymer distribution in green. For IND-C70, the number and size of IND-rich surface clusters significantly increase over the investigated storage time, from single, distinct entities first detected after 7 days, to the more pronounced, extensive APS/re-crystallisation observed after approximately 180 and 360 days of storage. Surface physical

instability and extensive cluster formation is even more evident in the images for IND-C85, the highest drug loading among those herein investigated for the IND-PVP ASD formulation.

Fig. 4B shows the quantified surface coverage of detected IND-rich domains as a function of storage time for the IND-C20, IND-C50, IND-C70 and IND-C85 IND-PVP ground, stored powder samples. As expected, the data indicate stronger APS/re-crystallisation tendencies and faster growth of IND surface coverage for higher drug loadings. The highest drug loading tested (IND-C85) exhibits a steep increase in the first 10 days, when the drug clusters cover up to $\sim$1.5% of the analysed surface, followed by slower APS/re-crystallisation that converges towards a maximum just below 6% of surface coverage (Fig. 4B). The coverage for IND-C70 remains stable below 0.5% for the first 30 days of storage (Fig. 4C) and thereafter the coverage values rise more slowly compared to IND-C85, which suggests that IND-C70 is kinetically more stable than IND-C85. IND-C70 reaches a surface coverage of $\sim$4% coverage after one year of storage. Conversely, the IND-C20 and IND-C50 extrudate powders exhibit a homogeneous distribution of the two components even after 6 and 12 months of storage: no IND-rich domains were detected on the surface of the aged IND-C20 particles, and only an average of $\sim$0.1% coverage was quantified on the aged IND-C50, suggesting higher kinetic stability for these ASD systems (Fig. 4D). A selection of additional ToF-SIMS images for IND-C20 and IND-C50 is provided in Fig. S9.

X-ray powder diffraction (XRPD) analyses were conducted on IND-C85 after 1, 7 and 22 months of storage for comparison with observed APS/re-crystallisation using ToF-SIMS. XRPD patterns for all measurements are reported in Fig. S13. The XRPD pattern at 1 month exhibits a broad amorphous halo, without any detectable crystalline peaks, suggesting that the sample is stable in its amor-

phous state. Only after 7 months small peaks start appearing, better observable after 22 months, indicating that crystalline content in the bulk and/or at the surface is present and increasing. The peaks correspond to $\gamma-$IND, whose simulated reference XRPD pattern is also included in Fig. S13 ([58]).

The classical Avrami model (Equation 1) and its modified version accounting for non-constant nucleation rate (Equation 2) were used to correlate the relative surface coverage ($\alpha_s(t)$) with the storage time (t) and to quantify the APS/re-crystallisation rate constants (k). The APS/re-crystallisation kinetics of IND-C70 presents an apparent sigmoidal distribution with a defined induction time period, later followed by a rapid increase in the coverage % dominated by APS/crystal nucleation and growth. The system dynamics are best described using the modified Avrami model (Equation 2, $n_A = 3$) for homogeneous nucleation and bi-dimensional growth of plate-like clusters as detected on the surface. For IND-C85, surface coverage data present no or only a very limited induction time period with a steep increase directly from day 0 (Fig. 4B), best modelled using Equation 1 with $n_A = 1$. This suggests the early presence of pre-nucleated IND-rich nano-clusters below the detection limit of the ToF-SIMS IP&A, and an immediate contribution of IND-rich domain growth constrained to needle and plate-like structures [55]. The quantified kinetic constants of the Avrami model were $k_{\mathrm{IND-C70}}$ of $2.52 \cdot 10^{-7}\mathrm{d}^{-1}$ and $k_{\mathrm{IND-C85}}$ of $1.73 \cdot 10^{-2}\mathrm{d}^{-1}$ for IND-C70 and IND-C85, respectively. IND-C20 and IND-C50 data were not fitted because they presented no or very low APS/crystallinity, and are only included as control points.

Changes in the population of detected IND-rich domains can be further quantified and visualised comparing the particle size distributions (PSDs) of these IND-rich domains detected on the surface of the ground powder samples across different storage times. Fig. 5 illustrates the cumulative area-based PSD (Q2)

of IND-C70 (A) and IND-C85 (B) for the investigated storage time of up to 360 days. The PSDs are consistently shifted to larger particle sizes, thus suggesting continuous growth even after 180 days. After an initial induction period, IND-C70 exhibits continuous nucleation and growth during the observed phase transition, which results in a continuous broadening of the PSD and a shift of the PSD towards larger particle sizes particularly for the largest size fractions (EqD $>$ 2 µm). After the first 90 days, the Q2D90 of IND-C70 increases by 1.44 µm (from 2.73 µm at 90 days to 4.17 µm at 360 days), while the Q2D25 remains approximately stable at $\sim$1.5 µm in the same time period. In comparison, IND-C85 presents a more uniform shift of the PSD, which indicates a short, initial, nucleation-dominated stage and a subsequent growth-dominated stage. Sub-micron API-rich domains are still observed for both IND-C70 and IND-C85 even after 360 days of storage, accounting for approximately 10% of the overall drug coverage area. These results indicate that amorphous phase separation and crystal nucleation still take place even after extensive storage times. Additional numerical data of the PSDs presented in Fig. 5 are provided in Table S5.

The quantified and area-normalised number of detected IND-rich domains ($n_{\mathrm{Obj}}/A_{\mathrm{ROI}}$) for IND-C70 and IND-C85 also provides an indication of the nucleation rate ($J(t)$) for each sample. The initial, constant nucleation rate ($J_0 = J(t{=}0)$ with $\alpha_s \cong 0$) was estimated to be $1.224 \cdot 10^{-03}$ µm$^{-2}d^{-1}$ for IND-C85, which is 2 orders of magnitude higher than the nucleation rate for IND-C70 of $1.429 \cdot 10^{-05}$ µm$^{-2}d^{-1}$. The fast nucleation kinetics of IND-C85 during this onset period aligns with earlier assumptions related to the presence of pre-nucleated IND-rich nano-clusters which quickly reach the detection limits of the ToF-SIMS IP&A within the first 5 days. For IND-C70, J_0 is significantly lower, which might be the result of an induction time period spreading APS/crystal nucle-

ation events over a longer time period of up to 180 days. The underlying trend is similar to the one seen for the surface coverage, with a clear distinction between these two drug loadings. Details regarding the calculation of J_0 are provided in the **supplementary information** (Section S1.4.3) with a image time-series in Fig. S11 showing detected IND-rich clusters and a plot in Fig. S12 for a direct visual comparison of the derived J_0 for IND-C70 and IND-C85, respectively.

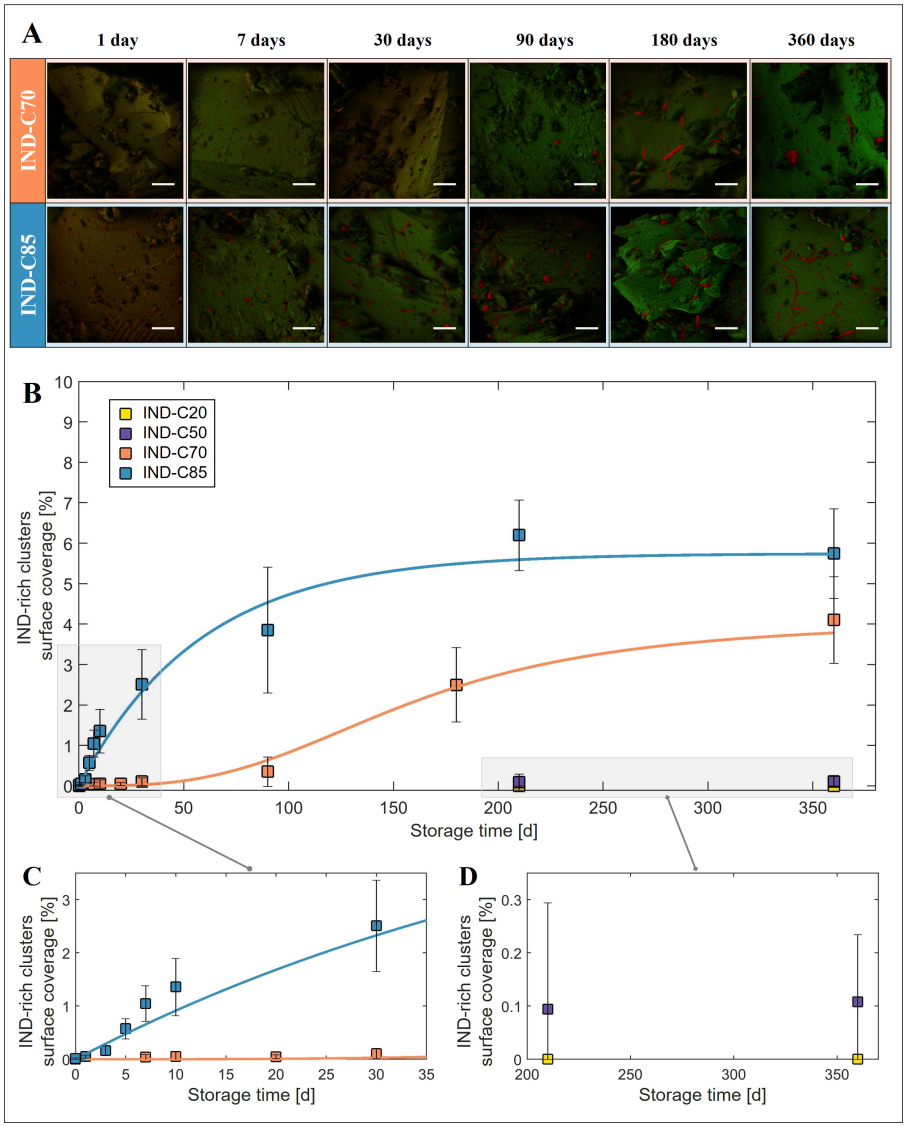

Figure 4: (A) Representative ToF-SIMS colour-overlay images of IND-C70 and IND-C85 ground powder samples. IND (identified by $C_{19}H_{17}ClNO_4^+$, $C_{19}H_{17}{}^{37}ClNO_4^+$, $C_7H_4ClO^+$, $C_7H_4{}^{37}ClO^+$, $C_6H_4Cl^+$, $C_6H_4{}^{37}Cl^+$) is shown in red, PVP ($C_6H_{10}NO^+$, $C_5H_8NO^+$, $C_4H_8NO^+$, $C_4H_5O^+$) in green. The corresponding greyscale images are provided in Fig. S10. Scale bar = 10 µm. (B) Quantified surface coverage of detected IND-rich domains over an investigated storage time of 360 days for IND-C20, IND-C50, IND-C70 and IND-C85. Error bars represent standard deviation from multiple ToF-SIMS images ($n_{Img} > 6$). The expanded views display (C) onset region (0 - 35 days) and (D) IND-C20 and IND-C50 low coverage values at 6 and 12 months.

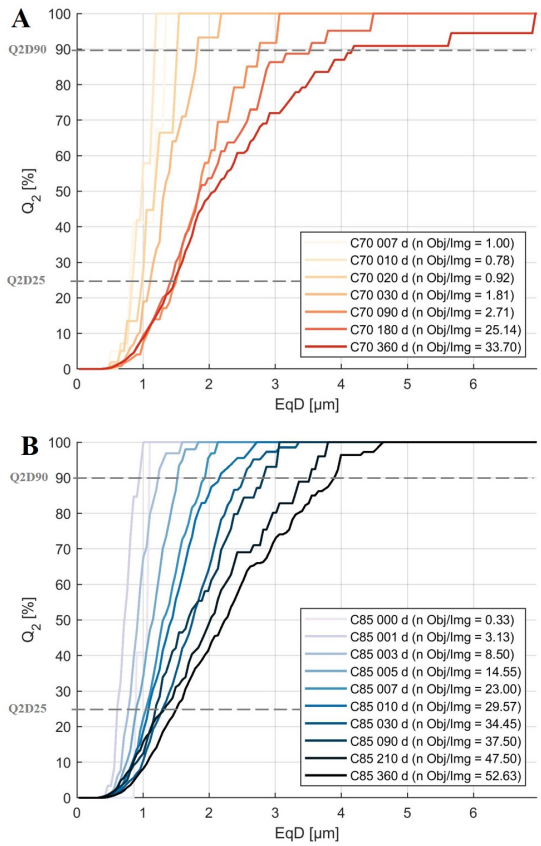

Figure 5: Cumulative particle size distribution of the API-rich domains detected on the surface of ground, stored ASD material for the IND-PVP formulations IND-C70 (A) and IND-C85 (B). The storage time and the average number of detected API-rich domains in each image are indicated in the insets.

4. Discussion: ToF-SIMS imaging and amorphous phase separation of ASD systems

Contrasting behaviours related to surface APS/re-crystallisation were observed for the two formulated drug systems investigated in this study. PCM-HPMC pellets exhibited fast formation of large PCM-rich domains, reaching 90% surface coverage within ∼30 days after HME for the PCM-C50 and for the PCM-C35 formulations. In comparison, IND-PVP ground material showed only modest surface APS/re-crystallisation with the appearance of isolated IND-rich domains leading to a surface coverage below 7% for IND-C85 and IND-C70 after ∼360 days. The results indicate that APS/re-crystallisation in ASDs is greatly affected by the re-crystallisation tendency/propensity of the specific drug candidate [23, 21]. PCM in its amorphous form is well known for being highly unstable, with re-crystallisation rates in the order of minutes at room temperature [62, 63, 41, 64]. Initial stages of amorphous phase separation leading to the formation of drug-rich domains became apparent using ToF-SIMS imaging within the first 24 hours after HME for PCM-HPMC (PCM-C35 and PCM-C50) and after 1 day of storage for IND-PVP (IND-C85), whilst a commonly employed technique such as XRPD did not show crystallinity on the corresponding samples for considerably longer time periods in the stability test (5 months for the PCM-C35 PCM-HPMC, Fig. S7 and 7 months for the IND-C85, Fig. S13). This discrepancy suggests that ToF-SIMS allows the detection of drug-rich domains before re-crystallisation occurs or that the total crystalline content at this early stage of the stability study remains below the XRPD detection limit of 1-5% w/w [27], leaving physical instability undetected using XRPD. The ability of ToF-SIMS to detect APS and its inherent high sensitivity are therefore particularly beneficial in the pharmaceutical industry during the *drug product development* phase, when it is crucial to reliably assess the stability of product

formulations at an early stage, and to promptly identify kinetically unstable systems leading to phase separation over the product's shelf life.

HME post-processing such as milling and grinding enhanced the APS/re-crystallisation kinetics in ASDs of IND-PVP comparing pelletised and ground material stored in the same conditions for up to 12 months, with the pellets showing good stability and the ground powder exhibiting a significant degree of APS/re-crystallisation. The increased APS/re-crystallisation in the ground powder material is possibly linked to the generation of mechanical stress and defects [61] during milling/grinding, as well as to the creation of a higher specific surface area in the ground powder that increases the probability of crystal nucleation and surface-enhanced re-crystallisation [63]. A careful risk assessment is therefore crucial to manufacture safe and reliable ASD formulations. ToF-SIMS can support faster process development through an earlier detection and an improved understanding on the impact of post-processing on ASD solid state stability.

The induction time after which surface APS/re-crystallisation was first observed was considerably reduced for the highest drug-loadings in both compound systems, suggesting the presence of pre-nucleation clusters shortly after HME. This behaviour highlights the supersaturated nature of these compositions and might indicate that the process conditions were not sufficient to eliminate these pre-nucleation clusters during HME for the highest drug-loadings. Nanometre-scale residual crystals, which could act as re-crystallisation *nuclei*, might not be detected by DSC and XRPD [26]. On the contrary ToF-SIMS, with its $\sim$200 nm spatial resolution, enabled the detection of sub-micron sized clusters. Both case studies highlight that the *APS/nucleation* phase continues, despite not being dominant, long after the *API-rich domain growth* phase has started (e.g. Fig. S3 and Fig. S12). This indicates a highly localised behaviour during APS/re-crystallisation where local drug-rich domains only deplete their direct

vicinity and further growth quickly becomes mass-transfer limited. In this context, the spatially resolved mass-spectral information from ToF-SIMS provide essential details on the local chemical homogeneity of solid pharmaceutical systems.

Combined with implemented IP&A methodologies for an automated and reliable quantification, the ToF-SIMS image data provide a means to elucidate underlying phase transformation mechanisms of amorphous phase separation, nucleation and crystal growth. Surface APS/re-crystallisation of the two ASD systems was successfully monitored and quantified over the course of the stability study to inform on phase transformation kinetics which were extracted using a (modified) Avrami model. IP&A further enables the extraction of size and shape descriptors such as the API-rich domain equivalent circle area diameter (EqD) and area (A_{Obj}). These were used to monitor changes in the particle size distribution which can be related to nucleation and growth phenomena. Tracking the total number of detected clusters overtime further revealed delayed/secondary events of amorphous phase separation and re-crystallisation, *i.e.* occurring at time-points at which crystal growth was simultaneously observed. Differences in the API-rich domain morphologies were observed in the high-resolution ToF-SIMS image data (e.g. spiral growth for PCM, needle-like for IND). Despite out of scope for this application, quantitative information on the crystal morphology can potentially be utilised to further distinguish between crystal polymorphs and better predict crystal growth kinetics.

The combined approach of using IP&A to support ToF-SIMS as an advanced surface characterisation technique with highly spatially resolved chemical information offered an effective opportunity to gain a better understanding of the surface APS/re-crystallisation mechanisms in ASDs. The presented ToF-SIMS methodologies have potential wider applicability outside of the pharmaceutical

product development, in other industrial areas. For instance, a better understanding and monitoring of surface instability can aid preventing corrosion in energy storage technologies, maintaining the favourable electric properties of amorphous semiconductor or avoiding loss of strength of amorphous metal alloys upon phase transformation in structural material applications.

5. Conclusions

This work demonstrates the combination of high resolution ToF-SIMS imaging and image analysis to monitor the physical stability of ASDs during stability testing and to extract quantitative information related to observed phase transformation kinetics. Formulations of two model substances were included in this study, IND-PVP and PCM-HPMC, each with four different drug loadings. The two compound systems exhibited extremely different surface amorphous phase separation/re-crystallisation behaviours: (1) the PCM-HPMC system presented a fast formation of extensive API-rich domains, which covered the surface of the high drug loading PCM-HPMC pellets within 1 month from HME; in comparison, (2) the IND-PVP system presented a more moderate surface physical instability, characterised by the formation of isolated, distinct needle-like IND-rich domains on the surface of the ground powder. Clear differences in the physical stability were observed characterising amorphous phase separation/re-crystallisation across multiple post-process manufacturing steps where applied mechanical stress for size reduction through grinding or milling and an increased specific surface area significantly promote local phase separation in IND formulations.

ToF-SIMS high spatial resolution and chemical sensitivity were key factors to assess the local chemical homogeneity of these multi-component solid phase systems and to indicate amorphous phase separation and re-crystallisation phe-

nomena already at an early stage of drug cluster formation. Notably, ToF-SIMS showed signs of physical instability significantly earlier than XRPD, a well established solid-state characterisation technique used to detect crystallinity. For the IND-PVP system, ToF-SIMS imaging provided evidence of surface physical instability within the first 24 hours from sample manufacturing, whilst XRPD detected signs of instability (crystallinity) only after approximately seven months. The developed ToF-SIMS characterization approach therefore enables an early assessment of phase separation tendencies and physical stability which is pivotal for a time-efficient formulation development of new pharmaceutical products which typically undergo long stability studies. Combined with advanced methodologies for data analysis, the quantitative information extracted from ToF-SIMS hyperspectral image data can provide crucial insights into the transformation dynamics during solid phase separation, helping to better understand limitations for kinetically stabilised ASD formulations. This supports the development of safe medicines at reduced costs due to faster pharmaceutical development times, which ultimately aims to benefit patients.

Data Statement

The developed MATLAB scripts and the data underpinning this publication will be available from the University of Strathclyde KnowledgeBase at `https://doi.org/10.15129/f9129326-dbb8-49b3-9a2d-c45da73f292a` from 2026 onwards, following the cessation of an embargo period. Further details relating to the data and the embargo can be accessed from the portal.

Contributions

E.P. conceived the study, performed all ToF-SIMS characterisation, analysed data and interpreted results, contributed to the IP&A routine, wrote the manuscript.

F.J.S.D. developed the IP&A routine, performed XRPD analysis for the IND-PVP systems, contributed to data interpretation and to the drafting of the manuscript. E.B. performed HME and XRPD for the PCM-HPMC systems. I.O. provided material for the IND-PVP systems. D.A.L., A.J.F. and G.W.H. provided funding. I.S.G. provided advice on ToF-SIMS measurements and interpretation, reviewed the manuscript. G.W.H. provided supervision and advice on formulation strategies, manufacturing, characterization and data interpretation, reviewed the manuscript. All authors approved the final manuscript.

Acknowledgement

The authors would like to thank the University of Strathclyde and the National Physical Laboratory (NPL) for funding researcher E.P.; the Engineering and Physical Sciences Research Council (EPSRC) for the studentships awarded to researchers F.J.S.D. (Grant Ref: EP/K503289/1) and E.B. (Grant Ref: EP/K503289/1); *The Wolfson Foundation* for financing the ToF-SIMS instrument based at the EPSRC Future Continuous Manufacturing and Advanced Crystallisation Research Hub. The authors also acknowledge that parts of this work was carried out in the CMAC National Facility supported by UKRPIF (UK Research Partnership Fund) award from the Higher Education Funding Council for England (HEFCE) (Grant Ref: HH13054). I.S.G acknowledges funding from the OrbiSIMS project in the Life-science and Health programme of the National Measurement System of the UK Department of Business, Energy and Industrial strategy.

Abbreviations

Acronym

API	Active pharmaceutical ingredient
APS	Amorphous phase separation
ASD	Amorphous solid dispersion
DSC	Differential scanning calorimetry
EqD	Equivalent circle area diameter
FoV	Field of view
HME	Hot melt extrusion
HPMC	Hydroxypropyl methylcellulose
HS	Hotspot
IND	Indomethacin
IP&A	Image processing and analysis
MSE	Mean squared error
m/z	*Mass-to-charge* ratio
PCM	Paracetamol
PDMS	Polydimethylsiloxane
PID	Primary ion dose
PSD	Particle size distribution
PVP	Polyvinylpyrrolidone
RH	Relative humidity
ROI	Region-of-interest
SEM	Scanning electron microscopy
T_{m}	Melting temperature
ToF-SIMS	Time of flight-secondary ion mass spectrometry
XRPD	X-ray powder diffraction
Symbols	
k	Avrami re-crystallisation rate constants
n_A	Avrami exponent

$\alpha_s(t)$	Relative crystalline fraction
J_0	Nucleation rate

Supplementary information

Structural formulae and repeat units of the chemicals used in the study and brief description of their function; positive polarity ToF-SIMS spectra of PCM, HPMC, IND and PVP reference powders and putative peak assignments; XRPD patterns for the PCM-HPMC and for the IND-PVP systems during storage; supplementary ToF-SIMS and optical microscopy images.

References

[1] Li-Feng Cui, Riccardo Ruffo, Candace K. Chan, Hailin Peng, and Yi Cui. Crystalline-amorphous core-shell silicon nanowires for high capacity and high current battery electrodes. *Nano Letters*, 9(1):491–495, 2009. ISSN 15306984. doi: 10.1021/nl8036323.

[2] Qing Li, Yuxia Xu, Shasha Zheng, Xiaotian Guo, Huaiguo Xue, and Huan Pang. Recent Progress in Some Amorphous Materials for Supercapacitors. *Small*, 14(28):1–19, 2018. ISSN 16136829. doi: 10.1002/smll.201800426.

[3] Shihan Yan, K. P. Abhilash, Lingyu Tang, Mei Yang, Yifan Ma, Qiuying Xia, Qiubo Guo, and Hui Xia. Research Advances of Amorphous Metal Oxides in Electrochemical Energy Storage and Conversion. *Small*, 15(4): 1–30, 2019. ISSN 16136829. doi: 10.1002/smll.201804371.

[4] Kenji Nomura, Hiromichi Ohta, Akihiro Takagi, Toshio Kamiya, Masahiro Hirano, and Hideo Hosono. Room-temperature fabrication of transparent flexible thin-film transistors using amorphous oxide semiconductors. *Nature*, 432:488–492, 2004. doi: 10.1038/nature03090. URL https://doi.org/10.1038/nature03090.

[5] Kazuo Morigaki and Chisato Ogihara. Amorphous Semiconductors: Structure, Optical, and Electrical Properties. In S. Kasap and P. Capper, editors, *Handbook of Electronic and Photonic Materials*, chapter 24, pages 557–571. Springer International Publishing, 2017. ISBN 9783319489339. doi: 10.1007/978-3-319-48933-9.

[6] W. Klement, R. Willens, and P. Duwez. Non-crystalline Structure in Solidified Gold–Silicon Alloys. *Nature*, 187(4740):869–870, 1960. doi: 10.1038/187869b0. URL https://doi.org/10.1038/187869b0.

[7] Akihisa Inoue. Stabilization of metallic supercooled liquid and bulk amorphous alloys. *Acta Materialia*, 48(1):279–306, 2000. ISSN 13596454. doi: 10.1016/S1359-6454(99)00300-6. URL https://doi.org/10.1016/S1359-6454(99)00300-6.

[8] Muhammad Mudasser Khan, Ali Nemati, Zia Ur Rahman, Umair Hussain Shah, Hassnain Asgar, and Waseem Haider. Recent Advancements in Bulk Metallic Glasses and Their Applications: A Review. *Critical Reviews in Solid State and Materials Sciences*, 43(3):233–268, 2018. ISSN 15476561. doi: 10.1080/10408436.2017.1358149. URL https://doi.org/10.1080/10408436.2017.1358149.

[9] Bruno C. Hancock and George Zografi. Characteristics and Significance of the Amorphous State in Pharmaceutical Systems. *Journal of Pharmaceutical Sciences*, 86(1):1–12, 1997. ISSN 00223549. doi: 10.1021/js9601896.

[10] Lian Yu. Amorphous pharmaceutical solids: Preparation, characterization and stabilization. *Advanced Drug Delivery Reviews*, 48(1):27–42, 2001. ISSN 0169409X. doi: 10.1016/S0169-409X(01)00098-9.

[11] Christian Leuner and Jennifer Dressman. Improving drug solubility for oral delivery using solid dispersions. *European Journal of Pharmaceutics and Biopharmaceutics*, 50(1):47–60, 2000. ISSN 09396411. doi: 10.1016/S0939-6411(00)00076-X.

[12] Guy Van Den Mooter. The use of amorphous solid dispersions: A formulation strategy to overcome poor solubility and dissolution rate. *Drug Discovery Today: Technologies*, 9(2):e79–e85, 2012. ISSN 17406749. doi: 10.1016/j.ddtec.2011.10.002. URL `http://dx.doi.org/10.1016/j.ddtec.2011.10.002`.

[13] Teófilo Vasconcelos, Bruno Sarmento, and Paulo Costa. Solid dispersions as strategy to improve oral bioavailability of poor water soluble drugs. *Drug Discovery Today*, 12(23-24):1068–1075, 2007. ISSN 13596446. doi: 10.1016/j.drudis.2007.09.005.

[14] Gordon L. Amidon, Hans Lennernäs, Vinod P. Shah, and John R. Crison. A Theoretical Basis for a Biopharmaceutic Drug Classification: The Correlation of in Vitro Drug Product Dissolution and in Vivo Bioavailability. *Pharmaceutical Research*, 12(3):413–420, 1995. ISSN 1573904X. doi: 10.1023/A:1016212804288.

[15] A. Newman. Rational design for amorphous solid dispersions. In Yihong Qiu, Yisheng Chen, Geoff Zhang, Lawrence Yu, and Rao V. Mantri, editors, *Developing Solid Oral Dosage Forms: Pharmaceutical Theory and Practice*, chapter 18, pages 497–518. Elsevier Inc., 2nd ed. edition, 2017. ISBN

9780128024478. doi: 10.1016/B978-0-12-802447-8.00018-2. URL http://dx.doi.org/10.1016/B978-0-12-802447-8.00018-2.

[16] Sandrien Janssens and Guy Van den Mooter. Review: physical chemistry of solid dispersions. *Journal of Pharmacy and Pharmacology*, 61(12):1571–1586, 2009. ISSN 00223573. doi: 10.1211/jpp/61.12.0001.

[17] Yanbin Huang and Wei-Guo Dai. Fundamental aspects of solid dispersion technology for poorly soluble drugs. *Acta Pharmaceutica Sinica B*, 4(1):18–25, 2014. ISSN 22113835. doi: 10.1016/j.apsb.2013.11.001. URL http://dx.doi.org/10.1016/j.apsb.2013.11.001.

[18] Tian Wu and Lian Yu. Surface crystallization of indomethacin below Tg. *Pharmaceutical Research*, 23(10):2350–2355, 2006. ISSN 07248741. doi: 10.1007/s11095-006-9023-4.

[19] Ye Sun, Lei Zhu, Tian Wu, Ting Cai, Erica M. Gunn, and Lian Yu. Stability of amorphous pharmaceutical solids: crystal growth mechanisms and effect of polymer additives. *AAPS Journal*, 14(3):380–388, 2012. ISSN 15507416. doi: 10.1208/s12248-012-9345-6.

[20] Ziyi Yang, Kathrin Nollenberger, Jessica Albers, Duncan Craig, and Sheng Qi. Molecular indicators of surface and bulk instability of hot melt extruded amorphous solid dispersions. *Pharmaceutical Research*, 32(4):1210–1228, 2015. ISSN 1573904X. doi: 10.1007/s11095-014-1527-8.

[21] Yuen Chuen Ng, Ziyi Yang, William James McAuley, and Sheng Qi. Stabilisation of amorphous drugs under high humidity using pharmaceutical thin films. *European Journal of Pharmaceutics and Biopharmaceutics*, 84(3):555–565, 2013. ISSN 09396411. doi: 10.1016/j.ejpb.2013.01.008. URL http://dx.doi.org/10.1016/j.ejpb.2013.01.008.

[22] ICH. Stability Testing of New Drug Substances and Products Q1A(R2), 2003.

[23] Jared A. Baird and Lynne S. Taylor. Evaluation of amorphous solid dispersion properties using thermal analysis techniques. *Advanced Drug Delivery Reviews*, 64(5):396–421, 2012. ISSN 0169409X. doi: 10.1016/j.addr.2011.07.009. URL http://dx.doi.org/10.1016/j.addr.2011.07.009.

[24] Yushen Guo, Evgenyi Shalaev, and Scott Smith. Physical stability of pharmaceutical formulations: Solid-state characterization of amorphous dispersions. *TrAC - Trends in Analytical Chemistry*, 49:137–144, 2013. ISSN 18793142. doi: 10.1016/j.trac.2013.06.002. URL http://dx.doi.org/10.1016/j.trac.2013.06.002.

[25] Xiangyu Ma and Robert O. Williams. Characterization of amorphous solid dispersions: An update. *Journal of Drug Delivery Science and Technology*, 50(January):113–124, 2019. ISSN 17732247. doi: 10.1016/j.jddst.2019.01.017.

[26] Dana E. Moseson, Naila A. Mugheirbi, Andrew A. Stewart, and Lynne S. Taylor. Nanometer-Scale Residual Crystals in a Hot Melt Extruded Amorphous Solid Dispersion: Characterization by Transmission Electron Microscopy. *Crystal Growth and Design*, 18(12):7633–7640, 2018. ISSN 15287505. doi: 10.1021/acs.cgd.8b01435.

[27] Justin A. Newman, Paul D. Schmitt, Scott J. Toth, Fengyuan Deng, Shijie Zhang, and Garth J. Simpson. Parts per Million Powder X-ray Diffraction. *Analytical Chemistry*, 87(21):10950–10955, 2015. ISSN 15206882. doi: 10.1021/acs.analchem.5b02758.

[28] Dana E. Moseson, Isaac D. Corum, Andres Lust, Kevin J. Altman, Tze Ning Hiew, Ayse Eren, Zoltan K. Nagy, and Lynne S. Taylor. Amorphous Solid

Dispersions Containing Residual Crystallinity: Competition Between Dissolution and Matrix Crystallization. *The AAPS Journal*, 23:69, 2021. ISSN 15507416. doi: 10.1208/s12248-021-00598-6.

[29] Mingyue Li, Wei Xu, and Yongchao Su. Solid-state NMR spectroscopy in pharmaceutical sciences. *TrAC Trends in Analytical Chemistry*, 135: 116152, 2021. ISSN 0165-9936. doi: https://doi.org/10.1016/j.trac.2020.116152. URL `https://www.sciencedirect.com/science/article/pii/S0165993620303812`.

[30] Feng Qian, Jun Huang, Qing Zhu, Raja Haddadin, John Gawel, Robert Garmise, and Munir Hussain. Is a distinctive single Tg a reliable indicator for the homogeneity of amorphous solid dispersion? *International Journal of Pharmaceutics*, 395(1-2):232–235, 2010. ISSN 03785173. doi: 10.1016/j.ijpharm.2010.05.033.

[31] Ziyi Yang, Kathrin Nollenberger, Jessica Albers, Jonathan Moffat, Duncan Craig, and Sheng Qi. The effect of processing on the surface physical stability of amorphous solid dispersions. *European Journal of Pharmaceutics and Biopharmaceutics*, 88(3):897–908, 2014. ISSN 18733441. doi: 10.1016/j.ejpb.2014.07.013. URL `http://dx.doi.org/10.1016/j.ejpb.2014.07.013`.

[32] Bernard Van Eerdenbrugh, Michael Lo, Kevin Kjoller, Curtis Marcott, and Lynne S Taylor. Nanoscale mid-infrared imaging of phase separation in a drug–polymer blend. *Journal of pharmaceutical sciences*, 101(6):2066–2073, 2012.

[33] Na Li and Lynne S Taylor. Nanoscale infrared, thermal, and mechanical characterization of telaprevir–polymer miscibility in amorphous solid dis-

persions prepared by solvent evaporation. *Molecular pharmaceutics*, 13(3): 1123–1136, 2016.

[34] Felix Kollmer, Wolfgang Paul, Martin Krehl, and Ewald Niehuis. Ultra high spatial resolution SIMS with cluster ions — approaching the physical limits. *Surface and Interface Analysis*, 45:312–314, 2013. doi: 10.1002/sia.5093.

[35] Felix Draude, Martin Körsgen, Andreas Pelster, Tanja Schwerdtle, Johannes Müthing, and Heinrich F. Arlinghaus. Characterization of freeze-fractured epithelial plasma membranes on nanometer scale with ToF-SIMS. *Analytical and Bioanalytical Chemistry*, 407:2203–2211, 2015. doi: 10.1007/s00216-014-8334-2.

[36] Shin Muramoto, Jeremy Brison, and David G. Castner. Exploring the surface sensitivity of TOF-secondary ion mass spectrometry by measuring the implantation and sampling depths of Bi n and C 60 ions in organic films. *Analytical Chemistry*, 84(1):365–372, 2012. ISSN 00032700. doi: 10.1021/ac202713k.

[37] Mani Ordoubadi, Florence K.A. Gregson, Hui Wang, Mark Nicholas, Sandra Gracin, David Lechuga-Ballesteros, Jonathan P. Reid, Warren H. Finlay, and Reinhard Vehring. On the particle formation of leucine in spray drying of inhalable microparticles. *International Journal of Pharmaceutics*, 592:120102, 2021. ISSN 0378-5173. doi: https://doi.org/10.1016/j.ijpharm.2020.120102. URL `https://www.sciencedirect.com/science/article/pii/S0378517320310875`.

[38] Mani Ordoubadi, Florence K.A. Gregson, Hui Wang, Nicholas B. Carrigy, Mark Nicholas, Sandra Gracin, David Lechuga-Ballesteros, Jonathan P. Reid, Warren H. Finlay, and Reinhard Vehring. Trileucine as a dispersibility enhancer of spray-dried inhalable microparticles. *Journal of Controlled*

Release, 336:522–536, 2021. ISSN 0168-3659. doi: https://doi.org/10.1016/j.jconrel.2021.06.045. URL https://www.sciencedirect.com/science/article/pii/S0168365921003436.

[39] Ivan J Hall Barrientos, Eleonora Paladino, Sarah Brozio, Melissa K Passarelli, Susan Moug, Richard A Black, Clive G Wilson, and Dimitrios A. Lamprou. Fabrication and characterisation of drug-loaded electrospun polymeric nanofibers for controlled release in hernia repair. *International Journal of Pharmaceutics*, 517(1-2):329–337, 2017. ISSN 03785173. doi: 10.1016/j.ijpharm.2016.12.022. URL https://doi.org/10.1016/j.ijpharm.2016.12.022.

[40] Ivan J Hall Barrientos, Eleonora Paladino, Peter Szabó, Sarah Brozio, and Peter J Hall. Using Type I Collagen to Modify Characteristics of Electrospun Polylactic Acid Nanofibers for Tissue Engineering Applications. *International Journal of Pharmaceutics*, 531:67–79, 2017. doi: 10.1016/j.ijpharm.2017.08.071. URL https://doi.org/10.1016/j.ijpharm.2017.08.071.

[41] Andreea Iuras, David J. Scurr, Catherine Boissier, Mark L. Nicholas, Clive J. Roberts, and Morgan R. Alexander. Imaging of Crystalline and Amorphous Surface Regions Using Time-of-Flight Secondary-Ion Mass Spectrometry (ToF-SIMS): Application to Pharmaceutical Materials. *Analytical Chemistry*, 88(7):3481–3487, 2016. ISSN 15206882. doi: 10.1021/acs.analchem.5b02621.

[42] Mark Nicholas, Mats Josefson, Magnus Fransson, Jonas Wilbs, Carl Roos, Catherine Boissier, and Kyrre Thalberg. Quantification of surface composition and surface structure of inhalation powders using TOF-SIMS. *International Journal of Pharmaceutics*, 587:119666, 2020. ISSN 03785173.

doi: 10.1016/j.ijpharm.2020.119666. URL https://doi.org/10.1016/j.ijpharm.2020.119666.

[43] Kyrre Thalberg, Foteini Papathanasiou, Magnus Fransson, and Mark Nicholas. Controlling the performance of adhesive mixtures for inhalation using mixing energy. *International Journal of Pharmaceutics*, 592(October 2020):120055, 2020. ISSN 18733476. doi: 10.1016/j.ijpharm.2020.120055. URL https://doi.org/10.1016/j.ijpharm.2020.120055.

[44] Frederik JS Doerr, Cameron J Brown, and Alastair J Florence. Direct image feature extraction and multivariate analysis for crystallization process characterization. *Crystal Growth & Design*, 2022.

[45] Frederik J S Doerr, Iain D H Oswald, and Alastair J Florence. Quantitative investigation of particle formation of a model pharmaceutical formulation using single droplet evaporation experiments and X-ray tomography. *Advanced Powder Technology*, 29(12):2996–3006, 2018. ISSN 0921-8831. doi: 10.1016/j.apt.2018.09.027. URL https://doi.org/10.1016/j.apt.2018.09.027.

[46] Frederik J.S. Doerr, Lee J. Burns, Becky Lee, Jeremy Hinds, Rebecca L. Davis-Harrison, Scott A. Frank, and Alastair J. Florence. Peptide Isolation via Spray Drying: Particle Formation, Process Design and Implementation for the Production of Spray Dried Glucagon. *Pharmaceutical Research*, 37 (12):1–19, 2020. ISSN 1573904X. doi: 10.1007/s11095-020-02942-5.

[47] Frederik J.S. Doerr and Alastair J. Florence. A micro-XRT Image Analysis and Machine Learning Methodology for the Characterisation of Multi-Particulate Capsule Formulations. *International Journal of Pharmaceutics: X*, 2:100041, 2020. ISSN 03785173. doi: 10.1016/j.ijpx.2020.100041. URL https://doi.org/10.1016/j.ijpx.2020.100041.

[48] Nikolaos Scoutaris, Andrew L. Hook, Paul R. Gellert, Clive J. Roberts, Morgan R. Alexander, and David J. Scurr. ToF-SIMS analysis of chemical heterogenities in inkjet micro-array printed drug/polymer formulations. *Journal of Materials Science: Materials in Medicine*, 23(2):385–391, 2012. ISSN 09574530. doi: 10.1007/s10856-011-4474-5.

[49] Ecaterina Bordos, Muhammad T. Islam, Alastair J. Florence, Gavin W. Halbert, and John Robertson. Use of Terahertz-Raman Spectroscopy to Determine Solubility of the Crystalline Active Pharmaceutical Ingredient in Polymeric Matrices during Hot Melt Extrusion. *Molecular Pharmaceutics*, 16(10):4361–4371, 2019. ISSN 15438392. doi: 10.1021/acs.molpharmaceut.9b00703.

[50] J. L S Lee, I. S. Gilmore, M. P. Seah, A. P. Levick, and A. G. Shard. Topography and field effects in secondary ion mass spectrometry Part II: Insulating samples. *Surface and Interface Analysis*, 44(2):238–245, 2012. ISSN 01422421. doi: 10.1002/sia.3833.

[51] F M Green, Ian S Gilmore, and Martin P Seah. TOF-SIMS : Accurate Mass Scale Calibration. *Journal of the American Society for Mass Spectrometry*, 17:514–523, 2006. doi: 10.1016/j.jasms.2005.12.005.

[52] Melvin Avrami. Kinetics of phase change. I General theory. *The Journal of Chemical Physics*, 7(12):1103–1112, 1939. ISSN 00219606. doi: 10.1063/1.1750380. URL `https://doi.org/10.1063/1.1750380`.

[53] Melvin Avrami. Kinetics of phase change. II Transformation-time relations for random distribution of nuclei. *The Journal of Chemical Physics*, 8(2):212–224, 1940. ISSN 00219606. doi: 10.1063/1.1750631. URL `https://doi.org/10.1063/1.1750631`.

[54] Melvin Avrami. Granulation, phase change, and microstructure kinetics of phase change. III. *The Journal of Chemical Physics*, 9(2):177–184, 1941. ISSN 00219606. doi: 10.1063/1.1750872. URL https://doi.org/10.1063/1.1750872.

[55] J W CHRISTIAN. CHAPTER 12 - Formal Theory of Transformation Kinetics. In J W CHRISTIAN, editor, *The Theory of Transformations in Metals and Alloys*, pages 529–552. Pergamon, Oxford, 2002. ISBN 978-0-08-044019-4. doi: 10.1016/B978-008044019-4/50016-7. URL http://www.sciencedirect.com/science/article/pii/B9780080440194500167https://doi.org/10.1016/B978-008044019-4/50016-7.

[56] Jiao Yang, Kristin Grey, and John Doney. An improved kinetics approach to describe the physical stability of amorphous solid dispersions. *International Journal of Pharmaceutics*, 384(1-2):24–31, 2010. ISSN 03785173. doi: 10.1016/j.ijpharm.2009.09.035.

[57] M. Haisa, S. Kashino, R. Kawai, and H. Maeda. The Monoclinic Form of p-Hydroxyacetanilide. *Acta Crystallographica Section B Structural Crystallography and Crystal Chemistry*, 32(4):1283–1285, apr 1976. ISSN 05677408. doi: 10.1107/S0567740876012223. URL https://doi.org/10.1107/S0567740876012223.

[58] Thomas J. Kistenmacher and Richard E. Marsh. Crystal and Molecular Structure of an Antiinflammatory Agent, Indomethacin, 1-(p-Chlorobenzoyl)-5-methoxy-2-methylindole-3-acetic Acid. *Journal of the American Chemical Society*, 94(4):1340–1345, 1972. ISSN 15205126. doi: 10.1021/ja00759a047.

[59] Paul A. Slavin, David B. Sheen, Evelyn E.A. Shepherd, John N. Sherwood,

Neil Feeder, Robert Docherty, and Snezena Milojevic. Morphological evaluation of the γ-polymorph of indomethacin. *Journal of Crystal Growth*, 237-239:300–305, 2002. ISSN 00220248. doi: 10.1016/S0022-0248(01)01924-8.

[60] Vlassios Andronis, Minoru Yoshioka, and George Zografi. Effects of sorbed water on the crystallization of indomethacin from the amorphous state. *Journal of Pharmaceutical Sciences*, 86(3):346–351, 1997. ISSN 00223549. doi: 10.1021/js9602711.

[61] Chandan Bhugra and Michael J. Pikal. Role of thermodynamic, molecular, and kinetic factors in crystallization from the amorphous state. *Journal of Pharmaceutical Sciences*, 97(4):1329–1349, 2008. ISSN 15206017. doi: 10.1002/jps.21138. URL `http://dx.doi.org/10.1002/jps.21138`.

[62] Deliang Zhou, Geoff G.Z. Zhang, Devalina Law, David J.W. Grant, and Eric A. Schmitt. Physical stability of amorphous pharmaceuticals: Importance of configurational thermodynamic quantities and molecular mobility. *Journal of Pharmaceutical Sciences*, 91(8):1863–1872, 2002. ISSN 00223549. doi: 10.1002/jps.10169. URL `http://dx.doi.org/10.1002/jps.10169`.

[63] Maxx Capece and Rajesh Davé. Enhanced physical stability of amorphous drug formulations via dry polymer coating. *Journal of Pharmaceutical Sciences*, 104(6):2076–2084, 2015. ISSN 15206017. doi: 10.1002/jps.24451.

[64] Jagadeesh Babu Nanubolu and Jonathan C. Burley. Investigating the recrystallization behavior of amorphous paracetamol by variable temperature Raman studies and surface raman mapping. *Molecular Pharmaceutics*, 9 (6):1544–1558, 2012. ISSN 15438384. doi: 10.1021/mp300035g.

[65] World Health Organization (WHO). WHO Model List of Essential

Medicines, 2019. URL https://apps.who.int/iris/handle/10665/325771.

[66] B. V. Robinson, F. M. Sullivan, J. F. Borzelleca, and S. L. Schwartz. *A Critical Review of the Kinetics and Toxicology of Polyvinylpyrrolidone (Povidone)*. Lewis Publishers, New York, 1st ed. edition, 1990. ISBN 9780873712880. URL https://doi.org/10.1201/9780203741672.

[67] Zubin B. Kuvadia and Michael F. Doherty. Spiral growth model for faceted crystals of non-centrosymmetric organic molecules grown from solution. *Crystal Growth and Design*, 11(7):2780–2802, 2011. ISSN 15287483. doi: 10.1021/cg101560u.

[68] Zubin B Kuvadia and Michael F Doherty. Reformulating multidimensional population balances for predicting crystal size and shape. *AIChE Journal*, 59(9):3468–3474, sep 2013. ISSN 00011541. doi: 10.1002/aic.14167. URL http://doi.wiley.com/10.1002/aic.14167.

[69] Jinjin Li and Michael F. Doherty. Steady state morphologies of paracetamol crystal from different solvents. *Crystal Growth and Design*, 17(2):659–670, 2017. ISSN 15287505. doi: 10.1021/acs.cgd.6b01510.

[70] Material: NaCl (ID: mp-22862). URL https://materialsproject.org/materials/mp-22862/.